Laser powder bed fusion of a pure tungsten ultra-fine single pinhole collimator for use in gamma ray detector characterisation

Authors: A. T. Sidambe[1,a] , D.S. Judson[2], S.J Colosimo[2,3], P. Fox[1]

1. Department of Mechanical, Materials and Aerospace Engineering, School of Engineering, University of Liverpool, Brownlow Hill, Liverpool, L69 3GH, United Kingdom
2. Department of Physics, University of Liverpool, Liverpool, L69 7ZE, United Kingdom
3. Cockcroft Institute, Sci-Tech Daresbury, University of Liverpool, Warrington, WA4 4AD United Kingdom

a. Corresponding author: Alfred T. Sidambe, Department of Mechanical, Materials & Aerospace Engineering, School of Engineering, University of Liverpool, Brownlow Hill, Liverpool, L69 3GH, United Kingdom, Email: A.Sidambe@liverpool.ac.uk, Tel: (+44) 0151 794 6832, Fax: (+44) 0151 794 4703

Abstract

Laser Powder Bed Fusion is a leading additive manufacturing technology, whose use has been recently extended to refractory metals such as tungsten. This work was carried out to manufacture a pure tungsten pinhole collimator that would otherwise be difficult to produce using conventional methods such as machining. The laser powder bed fusion process was used to produce an ultra-fine 0.5 mm diameter hole running along a 40 mm long beam stop component. A laser powder bed fusion scanning strategy (laser energy density of 348 J/mm^3) was selected with the aim of fabricating a high density tungsten component. The manufactured collimator was then used for gamma-ray detector characterisation. A collimated gamma-ray using a ^{241}Am source mounted on an automated scanning table was used to study the gamma-ray interaction with respect to position in a semiconductor detector, so that the position-dependent charge collection process could be characterised. The 0.5 mm diameter fine tungsten collimator yielded a relatively narrower beam spot, leading to more accurate scan results. However that was at the expense of number of gamma rays detected per second. Overall, the 0.5mm collimator allowed for higher resolution scans giving better detector characterisation results in comparison to a 1 mm diameter collimator.

Keywords: Laser Powder Bed Fusion, Selective Laser Melting, Tungsten, Refractory metals, Additive Manufacturing, Collimator, Gamma Radiation

1. Introduction and background

1.1. Additive Manufacturing

Laser Powder Bed Fusion (LPBF) is an additive manufacturing (AM) or 3D printing process that is increasingly being adopted by various industrial sectors to lower the cost of production of devices with complex shapes, particularly for high value low volume manufacturing [1]. The LPBF system consists of a laser source with a typical power of at least 200W which is used to fuse metal powder into a solid component using data from a sliced 3D CAD file, layer by layer. The layer thickness ranges from 30 to 50μm in size [2]. A schematic diagram of the LPBF process, also often referred to as Selective Laser Melting (SLM), is shown in Figure 1 [3].

The LPBF process has seen a rapid rise in recent years and has emerged as an alternative to conventional methods, such as machining and casting, in many applications which include nuclear medicine where components such as pinhole collimators are used. LPBF has the ability to manufacture complicated shaped parts with small dimensions, something which cannot be easily achieved using traditional techniques such as casting, forging, or machining [2, 3].

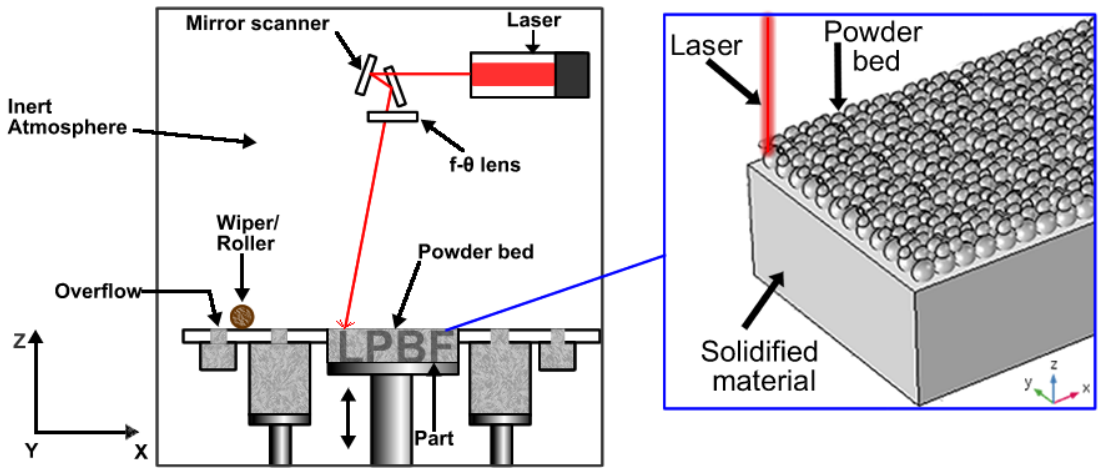

Figure 1: Schematic overview of selective laser powder bed fusion process.

1.2. Collimation

Collimator material needs to have a high atomic number to give good collimation of radiation beams such as gamma rays. The fabrication of components such as pinhole collimators used in radiation shielding applications and nuclear medicine is challenging because such devices are usually made from high-density materials such as tungsten and lead [4]. Tungsten offers improved shielding properties because the half value layer of tungsten is approximately 25% less than that of lead at the energies used in nuclear medicine [5]. However, tungsten has properties which make it difficult to process using traditional techniques [6].

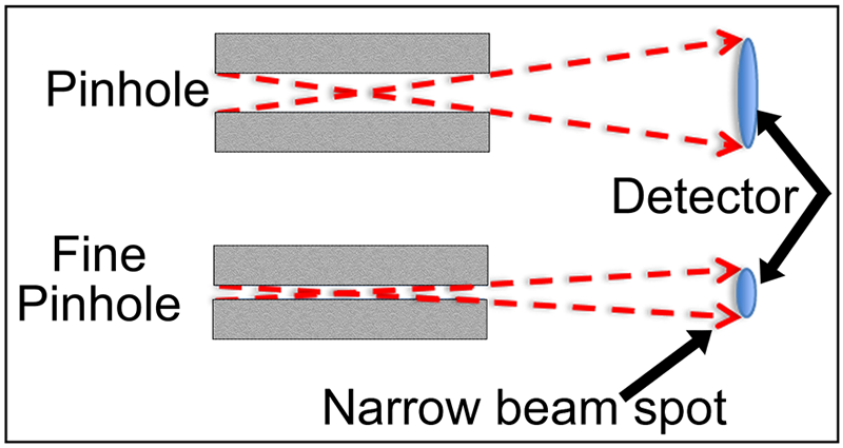

Figure 2: Schematic diagram of beam collimation.

LPBF on the other the other hand, has the potential to manufacture complicated shaped tungsten and to fabricate components such ultra-fine pinhole collimators. This is expected to lead to narrower beam spots and therefore more accurate scan results as illustrated in Figure 2. The processing of tungsten via LPBF, although technically challenging in its own right, can lead to an advantage in nuclear medicine and high value manufacturing. Table 1 shows the physical properties of tungsten which make it ideal for radiation shielding (density) but also render tungsten difficult to machine (DBTT) and challenging to process via LPBF (thermal conductivity, melt viscosity, surface tension). In addition to the above mentioned properties, optimisation of the processing of tungsten using LPBF also presents challenges because the process variables such as the laser scan speed, raw material powder, laser power, atmosphere, part design etc. all need to be optimised [7-11].

Physical properties	Tungsten
Density at 25 °C (g/cm^3)	19.2
Liquid Density (g/cm^3)	17.6
Melting Point (°C)	3422
Thermal Conductivity (W.m^{-1}.K^{-1})	174
Melt Viscosity (mPa.s)	8
Ductile-to-brittle transition temperature (DBTT) (°C)	250 to 400
Surface tension Force (N/m)	2.361

Table 1: Physical properties of tungsten [7, 12-15].

There have been a number of studies carried out in order to illustrate the potential of additive manufacturing of tungsten collimator components. In an early investigation, Zhong et al. [16] reported that pure tungsten powder could not be successfully melted due to the metal's high melting temperature. However, a collimator for an out-space hard X-ray modulation telescope was successfully fabricated using a tungsten nickel alloy powder in a directed energy deposition (DED) blown powder process (Laser Engineered Net Shaping: LENS™) [16]. A year later, Deprez et al. used LPBF to successfully fabricated a complex MR-compatible collimator with a large number of oblique pinholes from pure tungsten powder [4]. More recently, Samoudi et al. reported that 3D printed tungsten collimators are suited to be used for combined single photon emission computed tomography and magnetic resonance imaging (SPECT/MRI) systems and designed a full-ring multilofthole collimator that can be produced using LPBF [17]. Gear et al. have

shown that the LPBF processing parameters such as the scanning strategy can have an influence on the radiation attenuation properties of pure tungsten used in pinhole collimators [5, 18]. In this study, we have used the results from our developmental work [12, 15, 19], to manufacture a high density pure tungsten ultra-fine 0.5 mm diameter pinhole collimator that would otherwise be difficult to produce using conventional methods such as machining, expensive and labour intensive for electric discharge machining.

1.3. Radiation Detectors

Semiconductor radiation detectors are used in many applications such as nuclear medicine and health physics, homeland security, environmental monitoring, astronomy as well as fundamental physics research [20]. They offer excellent energy and position resolution allowing the characteristic gamma-ray energies released in nuclear decay to be used to identify the nuclear species present, even when the gamma-ray energies are within a few keV of each other. Semiconductor radiation detectors work by converting the energy of ionising radiation to an electrical current. Low energy (< 1 MeV) photons mainly interact with material either via Compton scattering or Photoelectric absorption [21]. These processes produce a high kinetic-energy electron. The high-energy electron then loses energy in the material, producing multiple electron-hole pairs until its total energy has been transferred to a cloud of charge carriers. The electron-hole pairs are created in the depletion region of

the semiconductor where electrons are excited into the valence band and holes are left in the conduction band. The total number of charge carriers produced is proportional to the energy deposited by the interacting radiation. An external bias voltage causes the free electron and holes to be drawn towards the positive and negative electrodes respectively. Here they induce a signal that can be read out and processed to give information on the total charge and thus energy deposited, as well as the charge collection process as a function of time.

The collecting electrodes can be electronically segmented to give information on the location of the interaction within the semiconductor. This is illustrated in Figure 3 below. A gamma-ray interaction causes negative electrons and positive holes to be created. These charge carriers are swept to the collecting electrodes by an electronic field induced by an external bias supply. 'γ-ray 1' will generate a cloud of electrons that will be swept under the influence of the electric field to the 1st positive electrode. 'γ-ray 2' would cause and electrical signal to be collected on both the third and fourth positive electrode. The exact size of the segments and the boundaries is a crucial input parameter for accurate detector modelling and thus accurate understanding of the charge collection process.

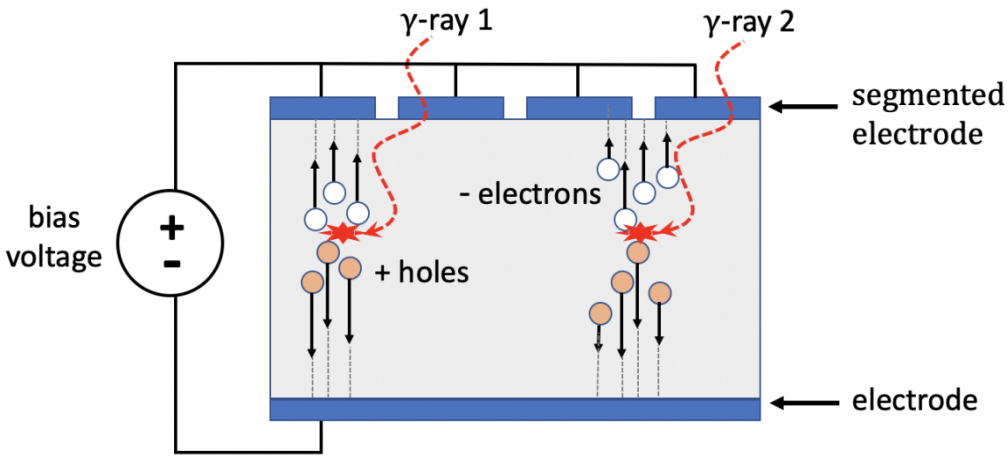

Figure 3: Simplified diagram showing the charge collection process with a segmented semiconductor detector.

The time dependence of the charge collection process depends heavily on factors such as the detector material, impurity concentration and gradient across the semiconductor as well as the detector geometry, electrode segmentation, and temperature all of which will affect the exact properties of the electric field and potential which, in turn, determine the characteristics of the generated electrical signal. Conversely, if the electrical properties are well understood, simulations can be used to infer position of interaction information from the observed charge collection signals. This is known as Pulse Shape Analysis (PSA) and is fundamental to the operation of many gamma-ray detectors and imaging devices (eg [20, 22, 23]). In this study, we have recorded the response of a semiconductor radiation detector as a function of gamma-ray interaction position in which the radiation source beam has been collimated using the ultra-fine pinhole LPBF tungsten collimator. This

approach enabled us to characterise the resolutions of the scans within the detector whilst comparing the response for a 1mm diameter collimator with that of the 0.5 mm diameter LPBF collimator.

1.3.1. Scanning detector bulk features

The fine 0.5 mm diameter LPBF collimator is expected to allow for higher precision measurements of certain features during detector scanning. Scanning the bulk of the detector material allows features of the detector mounting and housings to be observed that are not easy to identify and not necessarily provided by the manufacturer. For example, many semiconductor detectors are operated at cryogenic temperatures and so are mounted in an aluminium cryostat. Understanding the active detector area, holding structures and exact location of the detector within the cryostat is crucial to properly modelling the detector. An example of this is shown below in Figure 4. This shows the intensity variation across the surface of a Mirion (Canberra) SAGe well detector in both the xy and zy planes, measured using the 1.0 mm collimator. (Figure modified from [[21]].) The yellow band centred around x = y = 0 on the left image indicates the thickest region of active detector material (germanium). The thin blue circle of low counts within the yellow band shows the absorption / scattering of the incident gamma rays by the cryostat well. It is notable from this that the germanium crystal is not properly centred with respect to the cryostat. The bands of reduced intensity around z = 0 -15 mm and z = 20 - 30 mm on

the right-most image indicated the presence of a holding structure attenuating the gamma rays. These details are not readily provided by the manufacturer but are necessary to correctly model the detector's performance. The collimator size of 1.0 mm in diameter limits the resolution of the scan images and thus the minimum size of features that can be resolved. Therefore the 0.5 mm collimator allows for higher precision measurements of such features.

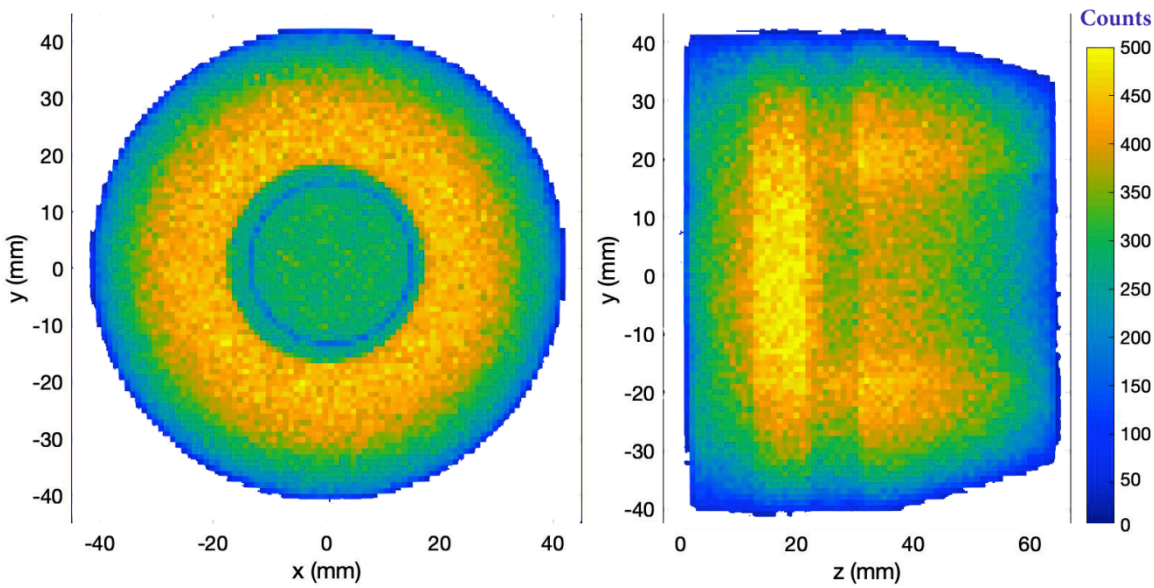

Figure 4: 1.0 mm collimator scan showing the uniformity of a Mirion (Canberra) SAGe well detector, Adapted from [21].

Figure 5 shows a scan of a germanium strip detector taken using a 1.0 mm collimator and ^{241}Am source of 60 keV gamma rays. The boundaries between the

active segments appear to be around 1 mm from this image but in reality, they are significantly smaller. The segments around Y = 93 - 97 mm, x > 80 mm show obvious charge collection deficiencies when compared to the other segment. The wide collimator aperture limits the ability to precisely study this feature. The 0.5 mm LPBF collimator will help to better understand the reduced intensity and the charge collection process at and around these boundaries.

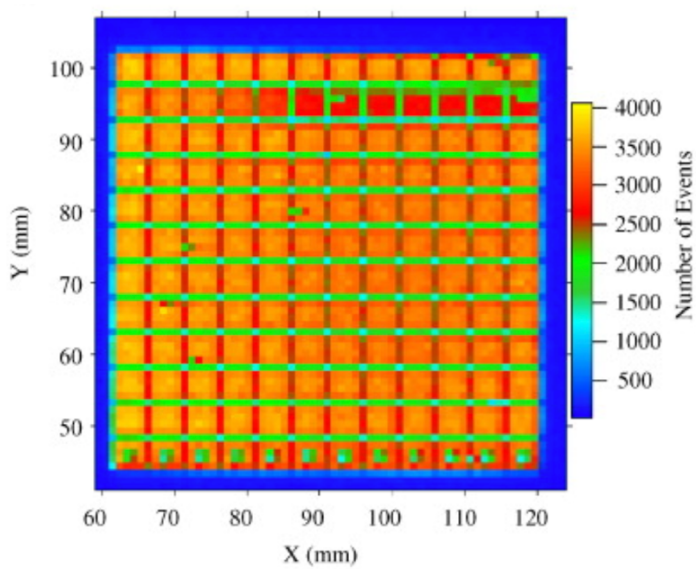

Figure 5: 1.0 mm scan of a segmented germanium detector. The region around Y=93-97 show clear charge collection issues. Taken from [24].

2. Experimental

2.1. Manufacturing of collimator

The LPBF process was carried by melting plasma-spheroidised commercial purity TEKMAT^{TM} W-45 tungsten powder supplied by Tekna Advanced Materials (Macon, France) in a Renishaw AM125 LPBF system (Stone, UK). Figure 6 (a) shows a scanning electron microscopic (SEM) image of the highly spherical morphology of the powder and Figure 6 (b) shows the powder particle distribution. SEM analysis was carried out using a Jeol 6610 (Akishima, Japan) scanning electron microscope at 20kV.

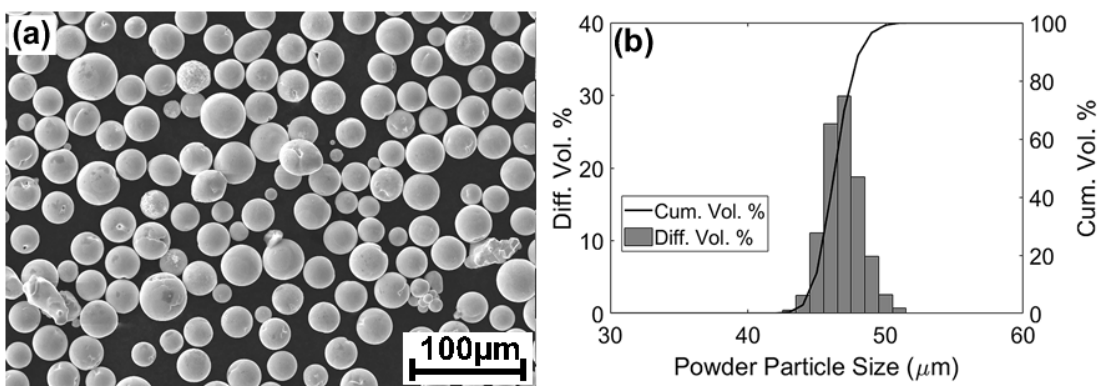

Figure 6: Powder morphology (a), powder particle distribution (b) for tungsten.

Hall Flow Test (sec/50g)	Tap Density (g/cm^3)	Apparent Density (g/cm^3)	Particle size distribution (µm)		
5	12.1	10.9	D10=25.2	D50=33.7	D90=48.4

Table 2: The table shows the physical properties of the tungsten powder.

Elements	W	Al	Ta	Ti	O	Mo	Others, each
(wt%)	>99.9	0.001	0.003	0.001	0.009	0.003	<0.001

Table 3: The table shows the chemical properties of the tungsten powder

Table 2 shows the physical properties, whereas Table 3 shows the chemical properties of the tungsten powder which was melted in an argon atmosphere with an initial residual oxygen content of less than 800 ppm (0.08 wt.%) within the chamber. The Renishaw AM125 system that was used operates on the principal of digital beam scanning and uses a high-powered ytterbium fibre laser, with a wavelength of 1070 nm, a maximum laser power of 200 W in continuous wave mode, a maximum laser scanning speed of 2000 mm/s and a laser beam diameter of 43µm at the target surface. The tungsten LPBF pinhole collimator was manufactured on a titanium substrate using a laser power of 200W with an exposure time of 200µs and point distance of 20µm. A hatch distance of 115µm and layer thickness of 50µm were also used, leading to a laser energy density of 348 J/mm^3.

The laser-based melting of the tungsten powder was carried out to fabricate the tungsten ultra-fine collimator as shown in Figure 7. The diameter of the pinhole within the collimator was designed to be 0.6 mm because in LPBF the surface roughness due to the powder source contributes to deviations in dimensions of up to

30% [25-28]. After fabrication, the powder entrapped in the pinhole was removed using a combination of drilling and ultrasonic vibrations. The resultant collimator diameter was measured using long plug pin gauges and SEM analysis. The surface topography of the fabricated tungsten collimator was also analysed using SEM.

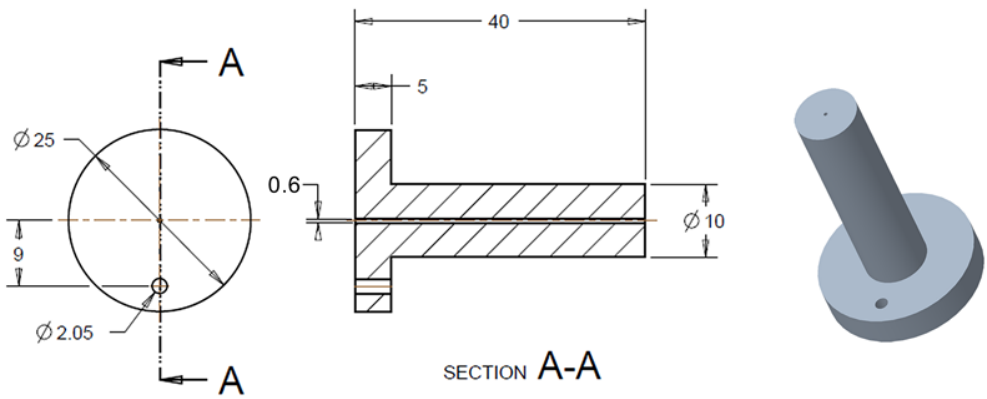

Figure 7: Drawing and CAD illustration of the collimator.

2.2. Collimated beam measurements

2.2.1. Detector scanning system

The detector scanning system (Nuclear Physics Department, University of Liverpool, UK) uses a source of gamma rays collimated into a pencil beam, mounted in an automated xy translational table combined with digital electronics to record a detector's response at known gamma-ray interaction positions. This is shown in Figure 8. Several monoenergetic gamma ray sources, including ^{241}Am (60 keV γ), ^{57}Co (121 keV γ) and ^{137}Cs (662 keV γ), can be used, giving a choice of incident

gamma-ray energies and thus average interaction depths. The collimated beam is scanned across the detector surface and a database of pulse shapes as a function of gamma-ray interaction position is recorded. This is then used to validate models of the detector signals e.g. [20, 22, 23]. Previously this has been performed using a 1.0 or 2.0 mm diameter collimator (e.g. [21, 24, 29]), giving a typical uncertainty of around 1.3 – 2.5 mm in the gamma-ray interaction position. This is typically sufficient for the bulk of the semiconductor material but is too large for the effective study of the process at segment boundaries which are typically 0.5 mm or less. The ultra-fine LPBF 0.5 mm collimator is expected to allow much more precise measurement of signals generated at these boundaries which is crucial to understand properties such as charge sharing and charge cloud size.

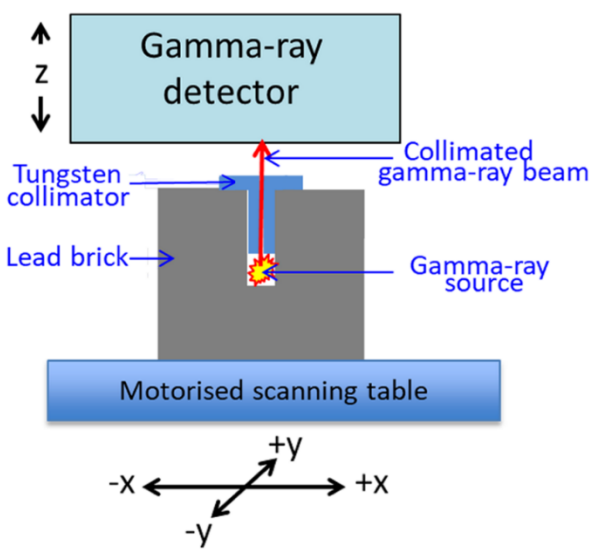

Figure 8: Diagram showing the detector scanning system.

For this study, scans were recorded using a ^{241}Am gamma ray source that had been collimated into a pencil beam by tungsten collimators. The partial scanning of a segmented germanium detector was carried out with different collimator arrangements of 1.0 mm collimator moved in 1.0 mm steps across the detector, a 1.0 mm collimator moved in 0.5 mm steps and the 0.5 mm LPBF collimator moved in 0.5 mm step sizes. This pencil beam was raster scanned across the detector surface via the automated scanning table. The detector signals induced by the charge collection process were then digitised, recorded and processed using digital electronics. The results were characterized using count rate.

3. Results and Discussion

3.1. LPBF Collimator and Pinhole Surfaces

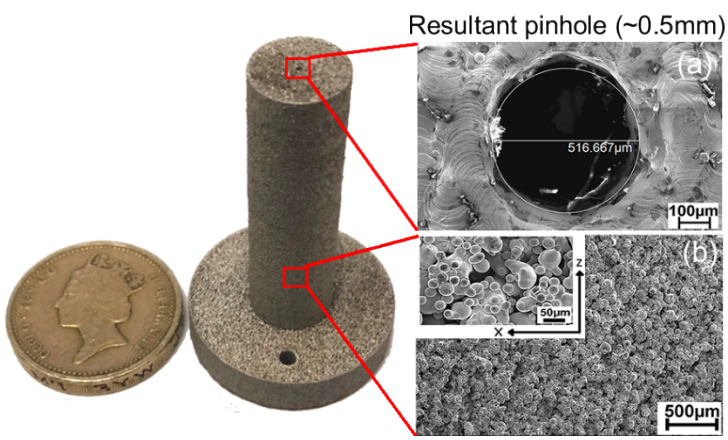

Figure 9: LPBF Collimator with the resultant ultra-fine pinhole (a) and typical vertical surface roughness of an as built LPBF tungsten part (b).

The tungsten collimator was fabricated without any visible defects or delamination during the melting process and a relatively smooth surface was produced. Figure 9 (a) shows a photograph of the LPBF collimator with the resultant ultra-fine pinhole. Also shown, in Figure 9 (b), is an SEM micrograph of the as built and typical vertical surface roughness of a LPBF tungsten part. The volume of unmelted adherent particles on the SEM in Figure 9 (b) contributed to the dimensional variations and production accuracy of the pinhole, leading to the final pinhole diameter of ~0.5 mm. These results were also compared to the measurements carried out using the long plug pin gauges and it was observed that the 0.5 mm gauge could fit tightly through the pinhole. On the other hand, a pin gauge of 0.6 mm diameter was not able to pass through the pinhole of the collimator. The impact of such deviation is dependent on the size of the feature and in this case, the relatively small dimension of the pinhole meant that the mean deviation was ~16%. The results of other bulk dimensions and differences between specified and produced object size of the LPBF collimator had no significant effect as the collimator was observed to readily fit on the lead shield's predesigned socket.

The LPBF strategies that can improve the dimensional accuracy and the surface roughness of the tungsten collimator include the use of powder particles with a lower particle size distribution (PSD) and selection of a lower layer thickness size. The collimator part was built to high density but LPBF offers the ability to build

lightweight or lower density parts where excess tungsten is not needed through hollow sections and lattice structures. Lower density tungsten has a lower conductivity, leading to less eddy currents which can be tailored for specific collimator applications [17]. However, the design of thin septal thicknesses with tungsten collimators has to take into consideration the susceptibility of tungsten to crack because of tungsten's ductile-to-brittle transition temperature shown in Table 1 [5], as well as wall thickness deviations which can be high [4].

3.2. Collimated beam measurements

Figure 10 shows a comparison of a partial scan of a segmented germanium detector with different collimators. Figure 10 (a) on the left was taken using a 1.0 mm collimator moved in 1.0 mm steps across the detector. Figure 10 (b) in the middle was taken using a 1.0 mm collimator and a 0.5 mm step size and Figure 10 (c) on the right image was taken using the 0.5 mm LPBF collimator and a 0.5 mm step size. The areas of high counts (>1400) show the active areas of the detector and the lines of reduced intensities show the segment boundaries. The number of counts detected at the segment boundaries using the 1.0 mm collimator was found to be relatively high, indicating that the collimated beam was larger than the segment boundaries and that active regions of the detector were being irradiated as well as the boundary region. When using the 0.5 mm LPBF collimator, the count rate at the boundary was close to zero indicating that the boundary region is of a similar size to

the collimated beam. The number of gamma rays per second through the 0.5 mm collimator was approximately a factor of 14 less than that through the 1.0 mm collimator so the time taken to acquire data at each step was increased by a factor of 14. Because of this, it is envisaged that a detector would first be scanned with the 1.0 mm collimator and then specific regions of interest would be probed using the 0.5 mm LPBF collimator.

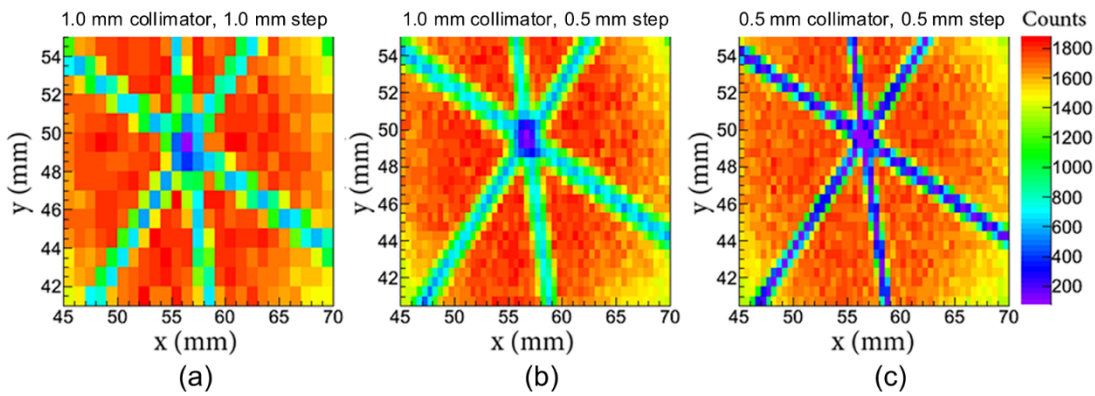

Figure 10: Scan results of a segmented germanium detector using different step sizes and collimator diameters. (a) 1.0 mm step size, 1.0 mm collimator, (b) 0.5 mm step size, 1.0 mm collimator, (c) 0.5 mm collimator, 0.5 mm step size.

4. Conclusion

In this study, the processing of a tungsten ultra-fine pinhole collimator was a success. The limitations to the effectiveness of LPBF processing of pure tungsten were overcame through the use of a laser energy density of 348 J/mm^3 to melt sub

45µm powder upon layer thicknesses of 50µm. The tungsten collimator device was expected to have a density of 98% [15]. The nominal collimator diameter was 0.6 mm and the resultant diameter was 0.5 mm due to variations of the LPBF process. The LPBF collimator was used, along with a standard 1.0 mm diameter collimator, to record scan using a ^{241}Am gamma ray source. The number of counts detected at the segment boundaries using the 1.0 mm collimator was found to be relatively high, indicating that the collimated beam was larger than the segment boundaries and that active regions of the detector were being irradiated as well as the boundary region. When using the 0.5 mm LPBF collimator, the count rate at the boundary was close to zero indicating that the boundary region is of a similar size to the collimated beam. The accuracy of the results, however, came at the expense of the number of gamma rays detected per second or detector count rate by a factor of 14. Therefore, the success of the process described in this work makes a valuable contribution to the sectors such as nuclear medicine.

5. Acknowledgements

The authors would like to thank the Engineering and Physical Sciences Research Council (EPSRC) for providing financial support under grant EP/K030884/1.

6. References

[1] Pogson SR, Fox P, Sutcliffe CJ, O'Neill W. The production of copper parts using

DMLR. Rapid Prototyping J. 2003;9:334-43.

[2] Sidambe AT. Effects of build orientation on 3D-printed Co-Cr-Mo: surface topography and L929 fibroblast cellular response. The International Journal of Advanced Manufacturing Technology. 2018;99:867-80. https://doi.org/10.1007/s00170-018-2473-0.

[3] Sidambe AT. Biocompatibility of Advanced Manufactured Titanium Implants-A Review. Materials. 2014;7:8168-88. https://doi.org/10.3390/ma7128168.

[4] Deprez K, Vandenberghe S, Van Audenhaege K, Van Vaerenbergh J, Van Holen R. Rapid additive manufacturing of MR compatible multipinhole collimators with selective laser melting of tungsten powder. Med Phys. 2013;40:012501. https://doi.org/10.1118/1.4769122.

[5] Gear JI, Taprogge J, White O, Flux GD. Characterisation of the attenuation properties of 3D-printed tungsten for use in gamma camera collimation. EJNMMI Physics. 2019;6:1. https://doi.org/10.1186/s40658-018-0238-3.

[6] Li R, Qin M, Liu C, Huang H, Lu H, Chen P, et al. Injection molding of tungsten powder treated by jet mill with high powder loading: A solution for fabrication of dense tungsten component at relative low temperature. International Journal of Refractory Metals and Hard Materials. 2017;62, Part A:42-6. https://doi.org/10.1016/j.ijrmhm.2016.10.015.

[7] Zhou X, Liu XH, Zhang DD, Shen ZJ, Liu W. Balling phenomena in selective laser melted tungsten. J Mater Process Tech. 2015;222:33-42.

https://doi.org/10.1016/j.jmatprotec.2015.02.032.

[8] Nie B, Yang L, Huang H, Bai S, Wan P, Liu J. Femtosecond laser additive manufacturing of iron and tungsten parts. Applied Physics A. 2015;119:1075-80.

[9] Bai S, Liu J, Yang P, Huang H, Yang L-M. Femtosecond fiber laser additive manufacturing of tungsten. SPIE LASE: International Society for Optics and Photonics; 2016. p. 97380U-U-10.

[10] Ivekovic A, Omidvari N, Vrancken B, Lietaert K, Thijs L, Vanmeensel K, et al. Selective laser melting of tungsten and tungsten alloys. International Journal of Refractory Metals and Hard Materials. 2017. https://doi.org/10.1016/j.ijrmhm.2017.12.005.

[11] Tan C, Zhou K, Ma W, Attard B, Zhang P, Kuang T. Selective laser melting of high-performance pure tungsten: parameter design, densification behavior and mechanical properties. Science and Technology of Advanced Materials. 2018:1-22. https://doi.org/10.1080/14686996.2018.1455154.

[12] Sidambe AT, Fox P. Interaction of pure tungsten powder with processing conditions in Selective Laser Melting. POWDERMET2017: International Conference on Powder Metallurgy and Particulate Materials. Las Vegas, Nevada: MPIF; 2017.

[13] Erik L, Wolf-Dieter S. Tungsten: properties, chemistry, technology of the element, alloys, and chemical compounds. New York: Plenum Publishers; 1999.

[14] Paradis P-F, Ishikawa T, Yoda S. Viscosity of liquid undercooled tungsten. J

Appl Phys. 2005;97:106101-1--3. https://doi.org/10.1063/1.1896432.

[15] Sidambe AT, Tian Y, Prangnell PB, Fox P. Effect of processing parameters on the densification, microstructure and crystallographic texture during the laser powder bed fusion of pure tungsten. International Journal of Refractory Metals and Hard Materials. 2018. https://doi.org/10.1016/j.ijrmhm.2018.10.004.

[16] Zhong M, Liu W, Ning G, Yang L, Chen Y. Laser direct manufacturing of tungsten nickel collimation component. J Mater Process Tech. 2004;147:167-73. https://doi.org/10.1016/j.jmatprotec.2003.12.009.

[17] Samoudi AM, Audenhaege KV, Vermeeren G, Verhoyen G, Martens L, Holen RV, et al. Simulated Design Strategies for SPECT Collimators to Reduce the Eddy Currents Induced by MRI Gradient Fields. IEEE Transactions on Nuclear Science. 2015;62:2017-22. https://doi.org/10.1109/TNS.2015.2476601.

[18] Gear J, Flux G. Design Optimisation of 3D Printed Parallel-Hole Tungsten Collimators for High Activity I-131 Imaging. SPRINGER 233 SPRING ST, NEW YORK, NY 10013 USA. p. S112-S.

[19] Sidambe AT, Fox P. Investigation of the Selective Laser Melting process with tungsten metal powder. 19th Plansee Seminar. Reutte, Austria: Plansee; 2017.

[20] Tsoulfanidis N. Measurement and detection of radiation: CRC press; 2010.

[21] Unsworth C, Boston AJ, Boston HC, Harkness-Brennan LJ, Judson DS, Nolan PJ, et al. Characterisation of a small electrode HPGe detector. Nuclear Instruments and Methods in Physics Research Section A: Accelerators, Spectrometers, Detectors

and Associated Equipment. 2019;927:293-300. https://doi.org/10.1016/j.nima.2019.02.043.

[22] Bruyneel B, Birkenbach B, Reiter P. Space charge reconstruction in highly segmented HPGe detectors through capacitance-voltage measurements. Nuclear Instruments and Methods in Physics Research Section A: Accelerators, Spectrometers, Detectors and Associated Equipment. 2011;641:92-100. https://doi.org/10.1016/j.nima.2011.02.110.

[23] Wright JP, Harkness-Brennan LJ, Boston AJ, Judson DS, Labiche M, Nolan PJ, et al. Position resolution simulations for the inverted-coaxial germanium detector, SIGMA. Nuclear Instruments and Methods in Physics Research Section A: Accelerators, Spectrometers, Detectors and Associated Equipment. 2018;892:84-92. https://doi.org/10.1016/j.nima.2018.02.106.

[24] Boston HC, Boston AJ, Cooper RJ, Cresswell J, Grint AN, Mather AR, et al. Characterisation of the SmartPET planar Germanium detectors. Nuclear Instruments and Methods in Physics Research Section A: Accelerators, Spectrometers, Detectors and Associated Equipment. 2007;579:104-7. https://doi.org/10.1016/j.nima.2007.04.017.

[25] Xiang Z, Wang L, Yang C, Yin M, Yin G. Analysis of the quality of slope surface in selective laser melting process by simulation and experiments. Optik. 2019;176:68-77. https://doi.org/10.1016/j.ijleo.2018.09.049.

[26] Mumtaz K, Hopkinson N. Top surface and side roughness of Inconel 625 parts

processed using selective laser melting. Rapid Prototyping J. 2009;15:96-103. https://doi.org/10.1108/13552540910943397.

[27] Sidambe AT. Three dimensional surface topography characterization of the electron beam melted Ti6Al4V. Metal Powder Report. 2017;72:200-5. https://doi.org/10.1016/j.mprp.2017.02.003.

[28] Sidambe AT, Todd I, Hatton PV. Effects of build orientation induced surface modifications on the in vitro biocompatibility of electron beam melted Ti6Al4V. Powder Metall. 2016;59:57-65. https://doi.org/10.1080/00325899.2016.1153278.

[29] Harkness-Brennan LJ, Judson DS, Boston AJ, Boston HC, Colosimo SJ, Cresswell JR, et al. An experimental characterisation of a Broad Energy Germanium detector. Nuclear Instruments and Methods in Physics Research Section A: Accelerators, Spectrometers, Detectors and Associated Equipment. 2014;760:28-39. https://doi.org/10.1016/j.nima.2014.05.080.

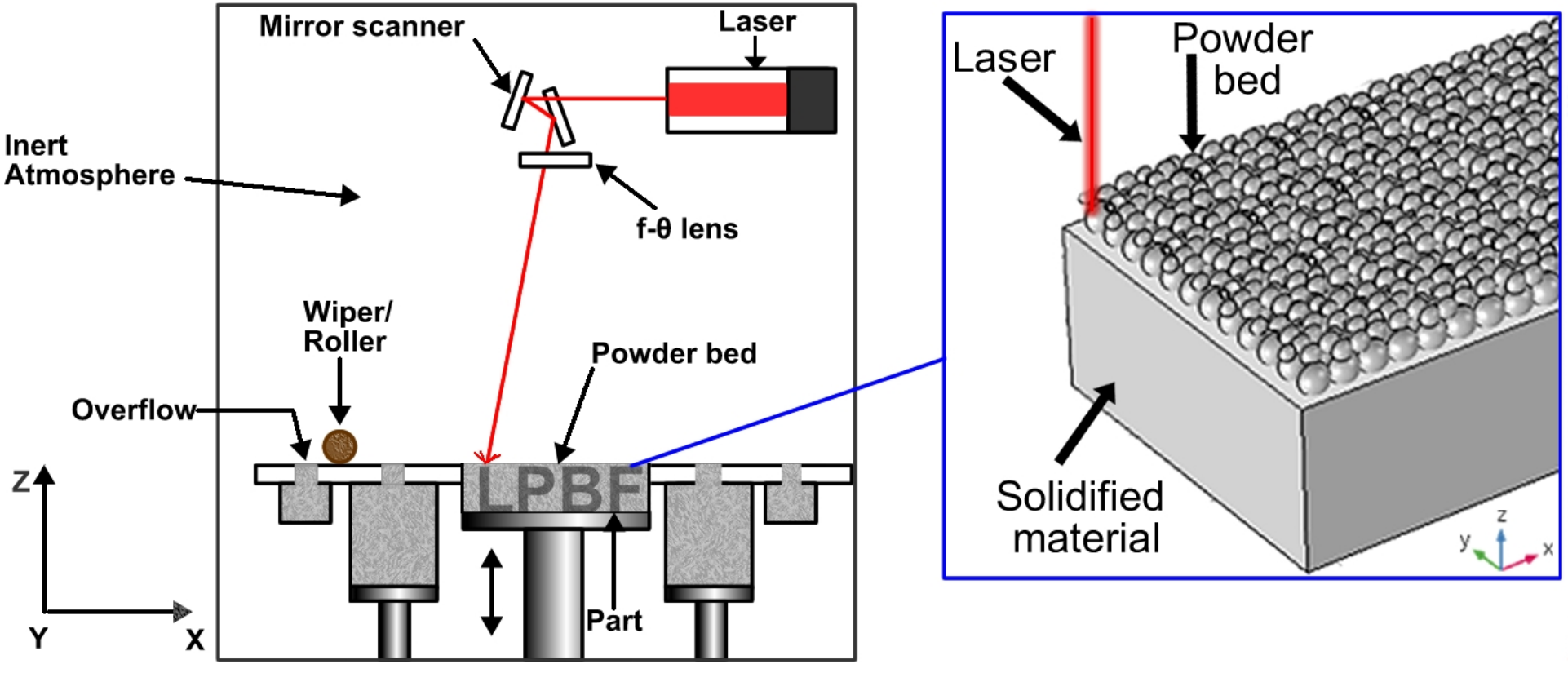
Mirror scanner
Laser
Inert
Atmosphere
f-θ lens
Wiper/
Roller
Powder bed
Overflow
LPBF
Z
Y
X
Part
Laser
Powder
bed
Solidified
material
z
y
x

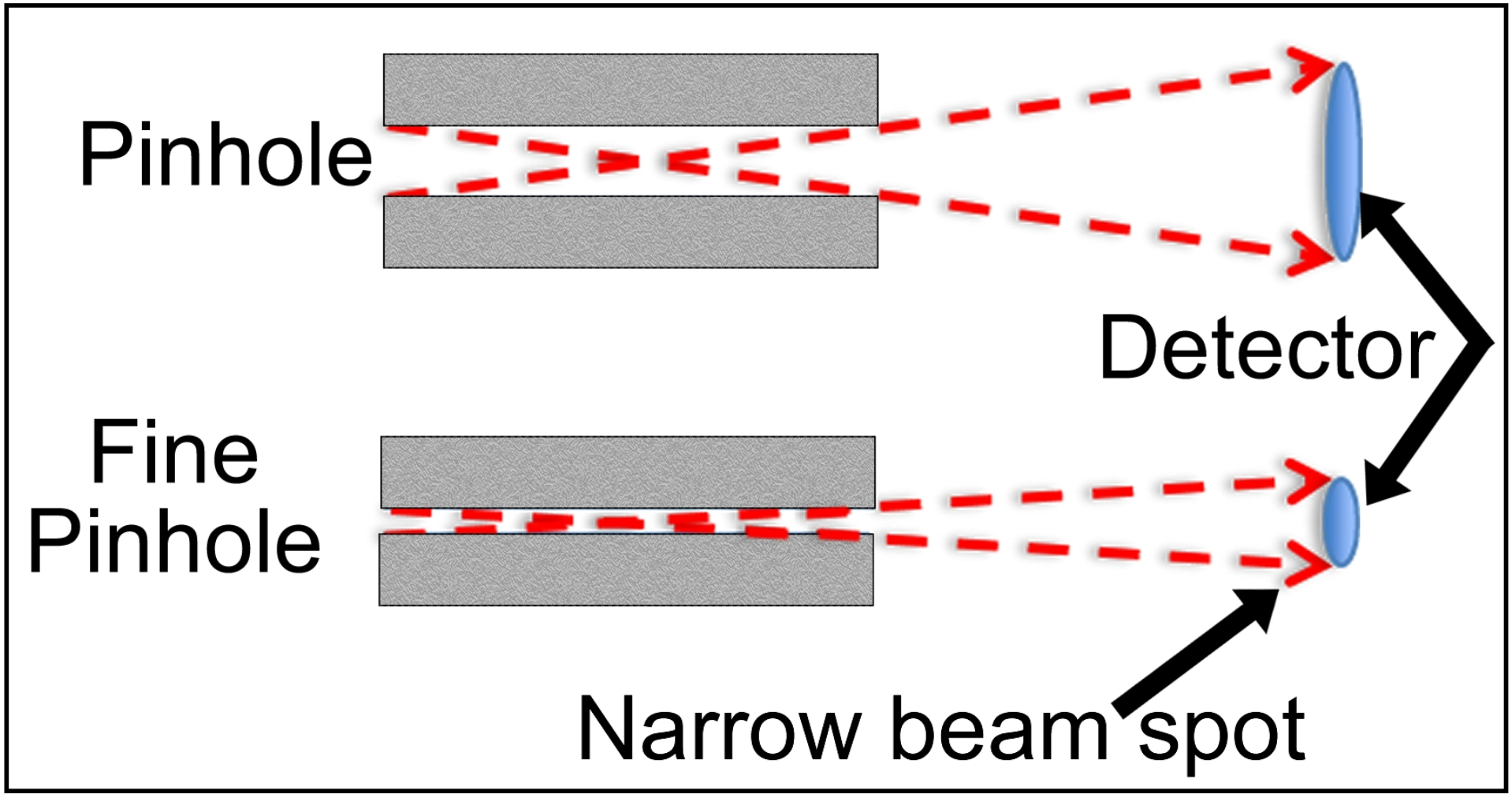
Pinhole
Detector
Fine
Pinhole
Narrow beam spot

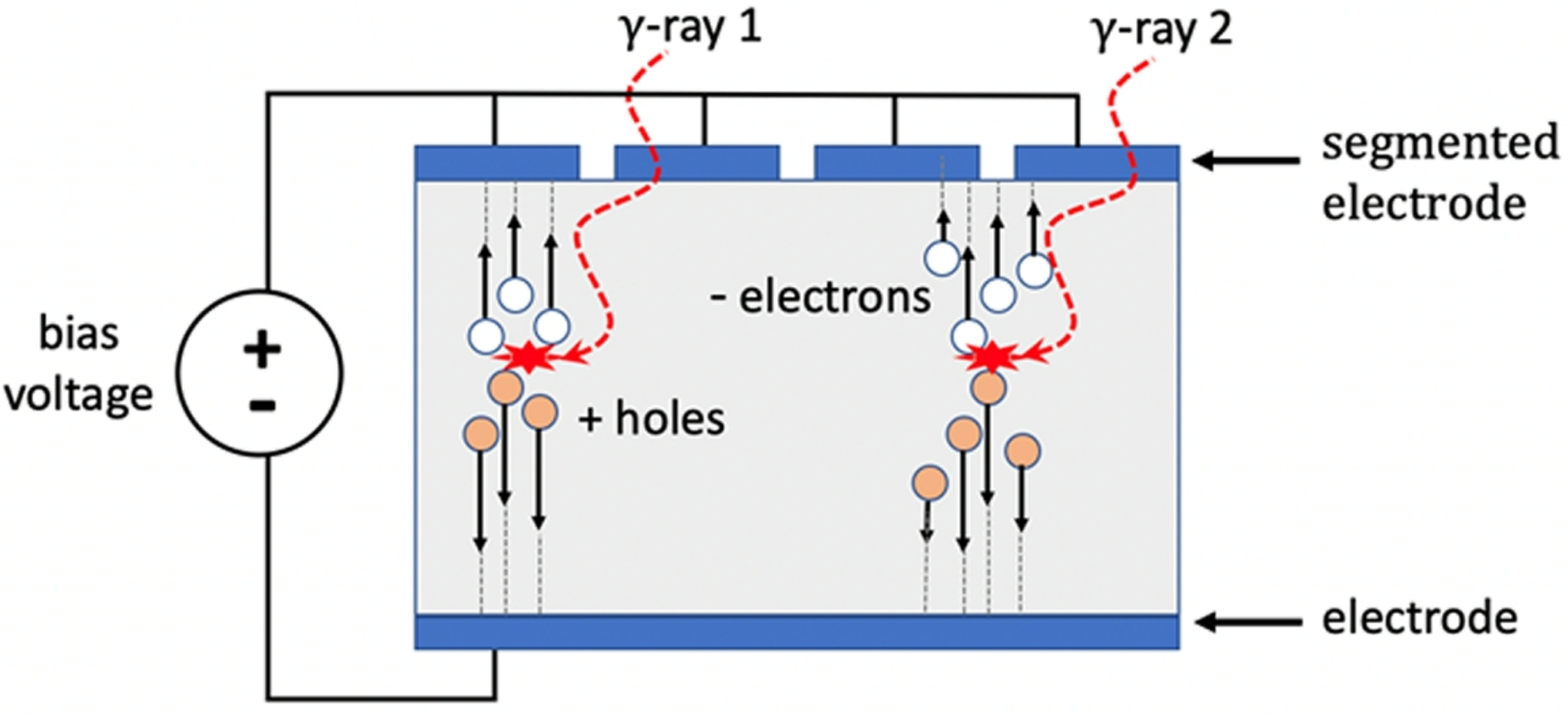
γ-ray 1
γ-ray 2
segmented electrode
bias voltage
+
-
- electrons
+ holes
electrode

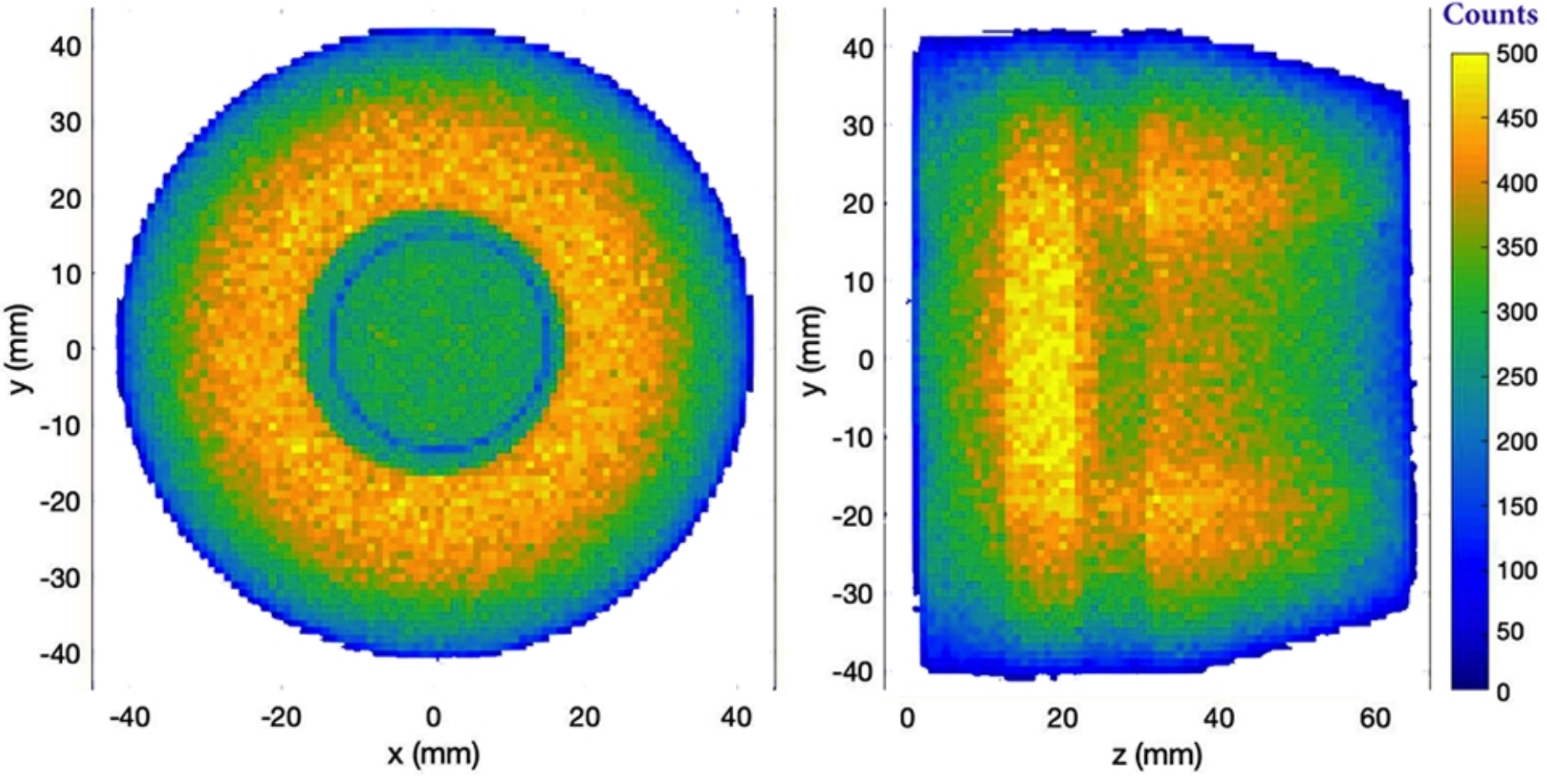
y (mm)
x (mm)
z (mm)
Counts
500
450
400
350
300
250
200
150
100
50
0
40
30
20
10
0
-10
-20
-30
-40
-40
-20
0
20
40
60

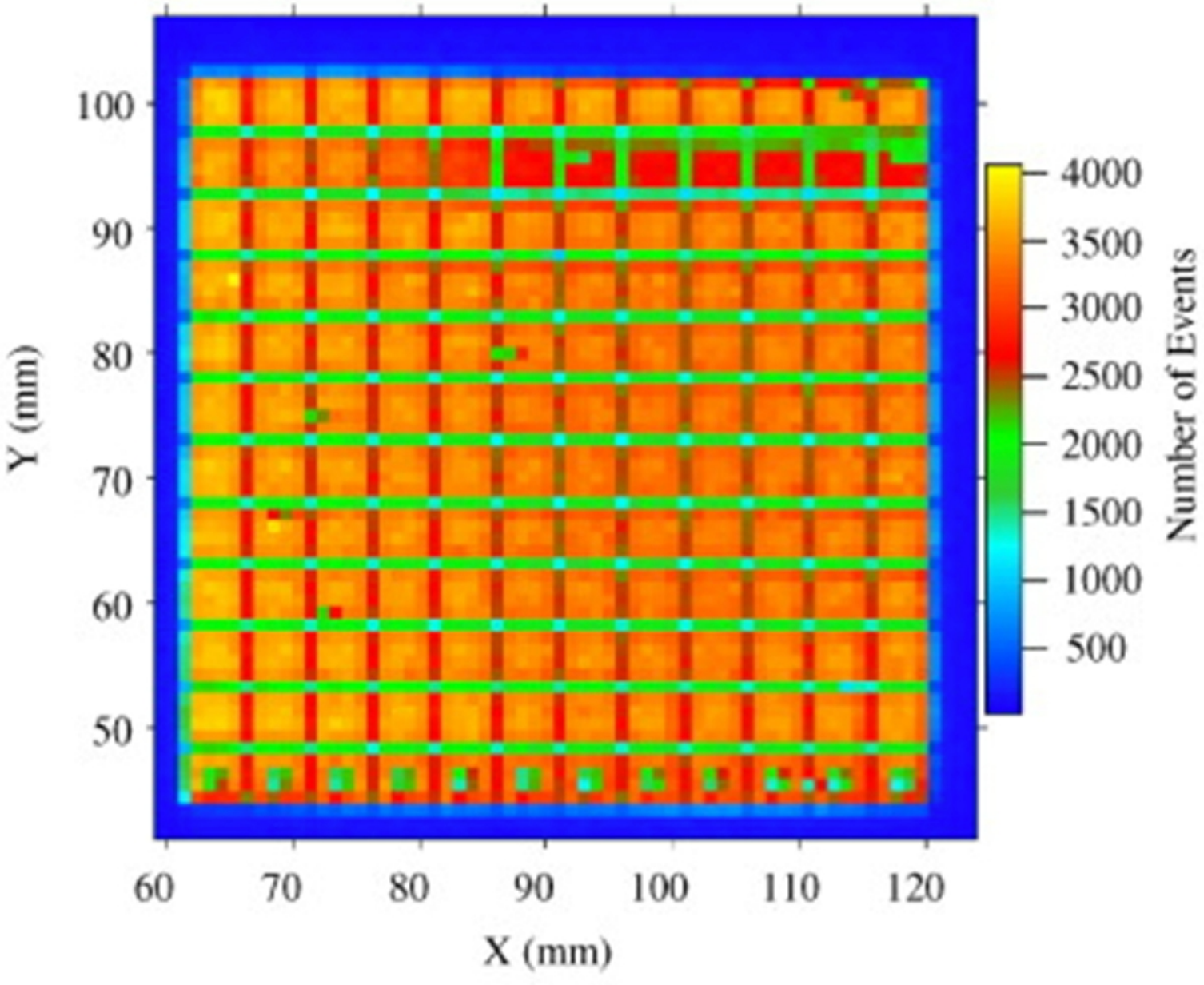
100
90
80
70
60
50
Y (mm)
60
70
80
90
100
110
120
X (mm)
4000
3500
3000
2500
2000
1500
1000
500
Number of Events

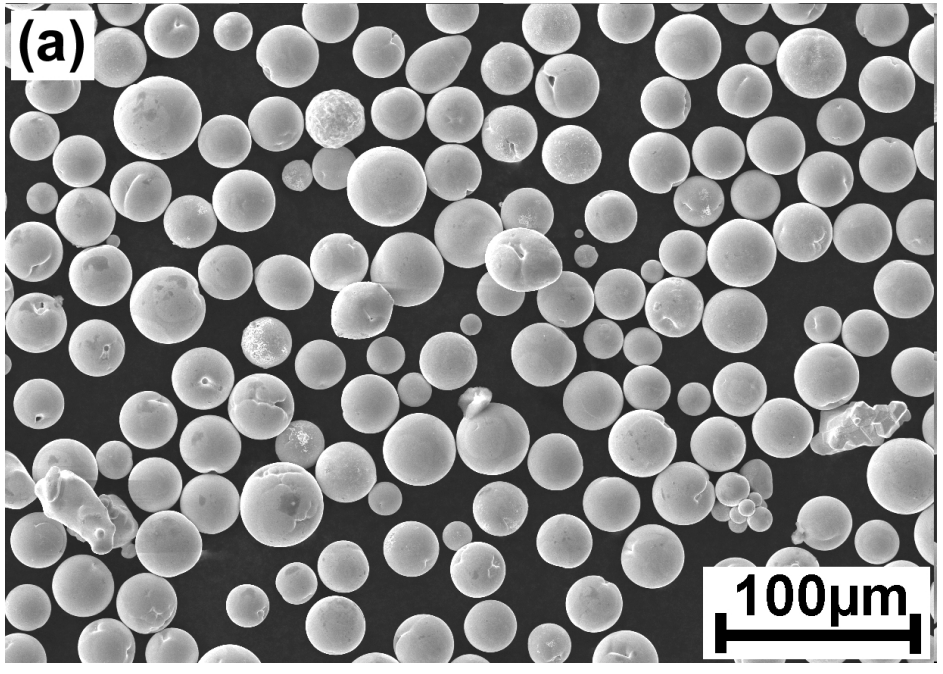
(a)
100μm

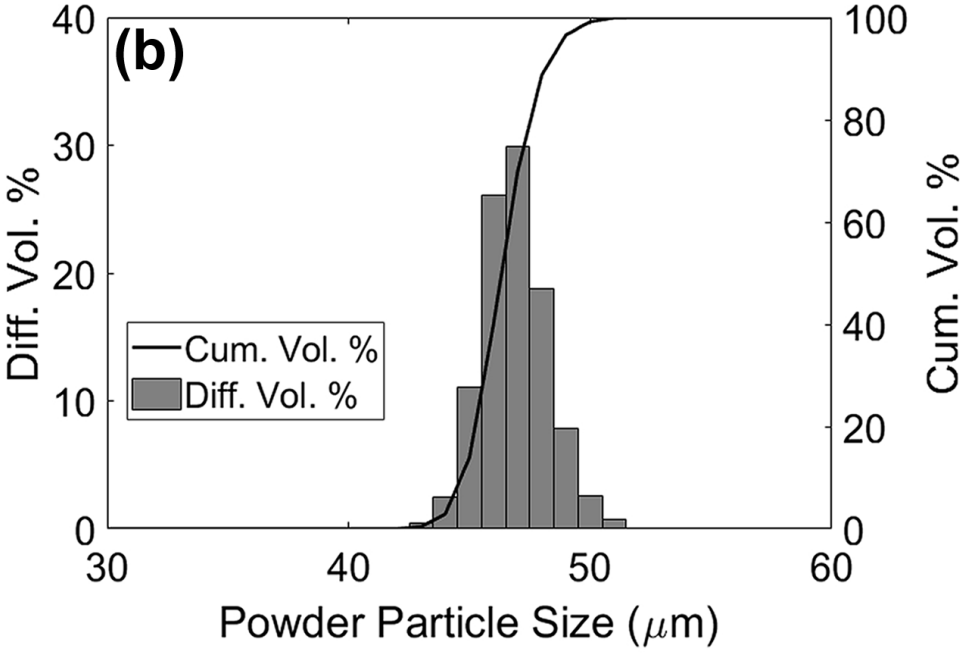
(b)
Diff. Vol. %
Cum. Vol. %
Cum. Vol. %
Diff. Vol. %
Powder Particle Size (μm)
0
10
20
30
40
0
20
40
60
80
100
30
40
50
60

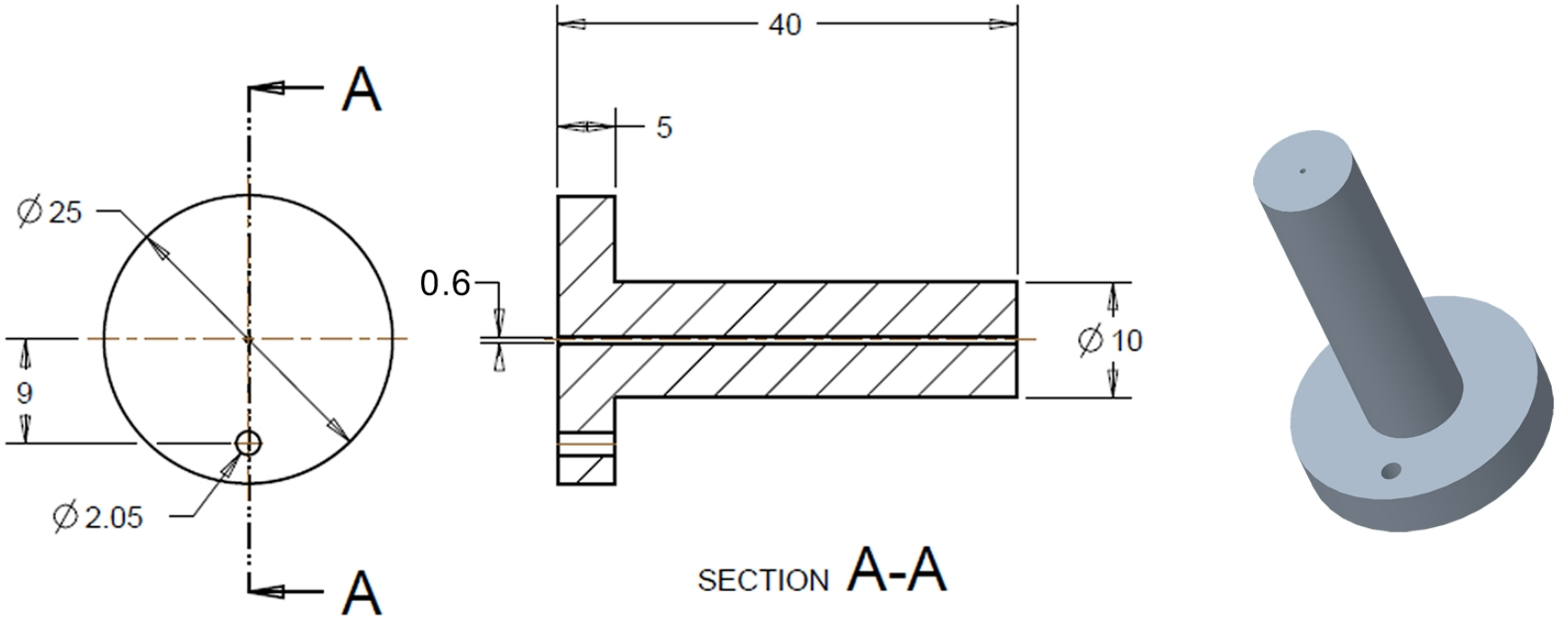
A
∅25
9
∅2.05
A
40
5
0.6
∅10
SECTION A-A

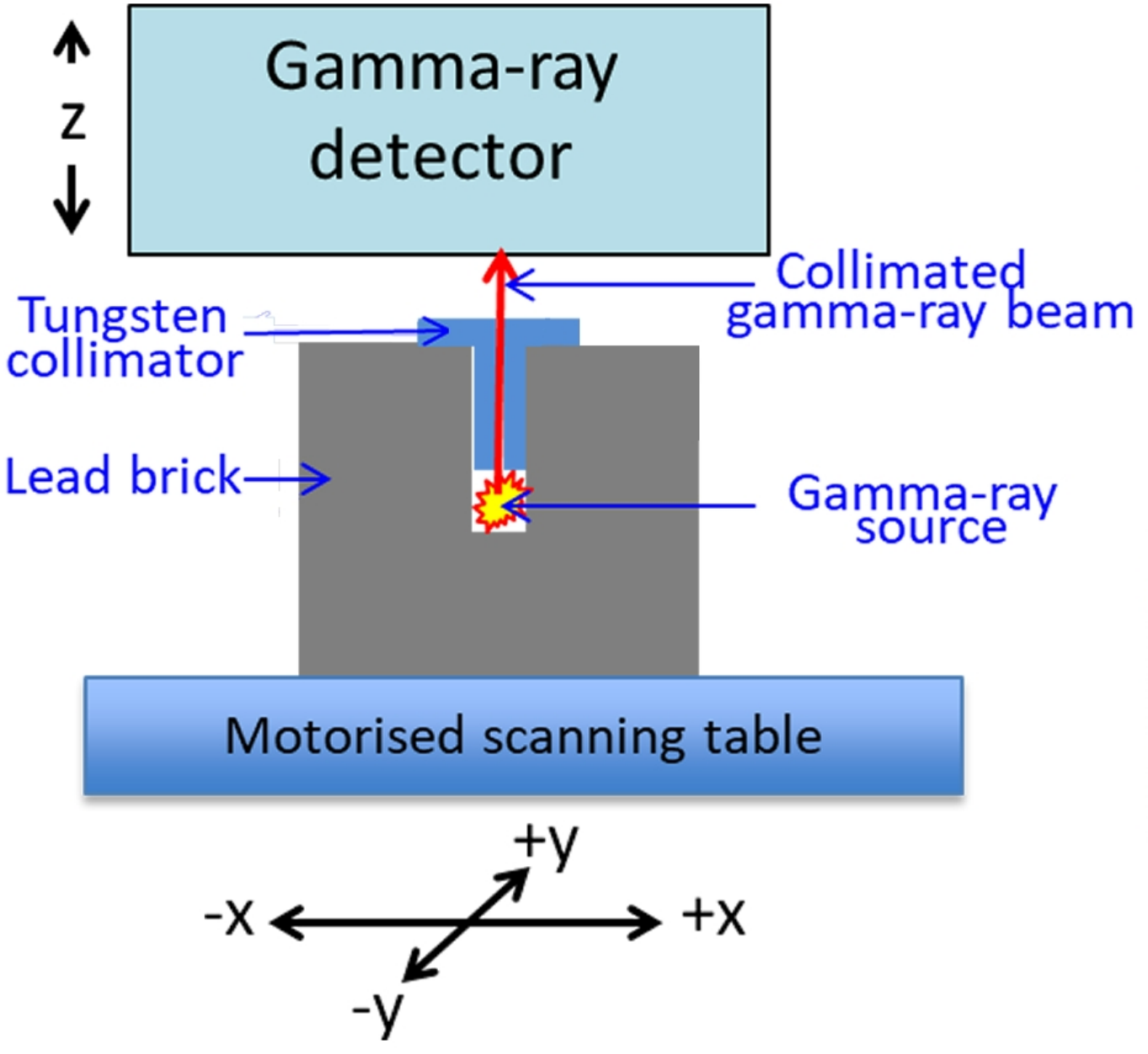
Gamma-ray detector
z
Collimated gamma-ray beam
Tungsten collimator
Lead brick
Gamma-ray source
Motorised scanning table
+y
-x
+x
-y

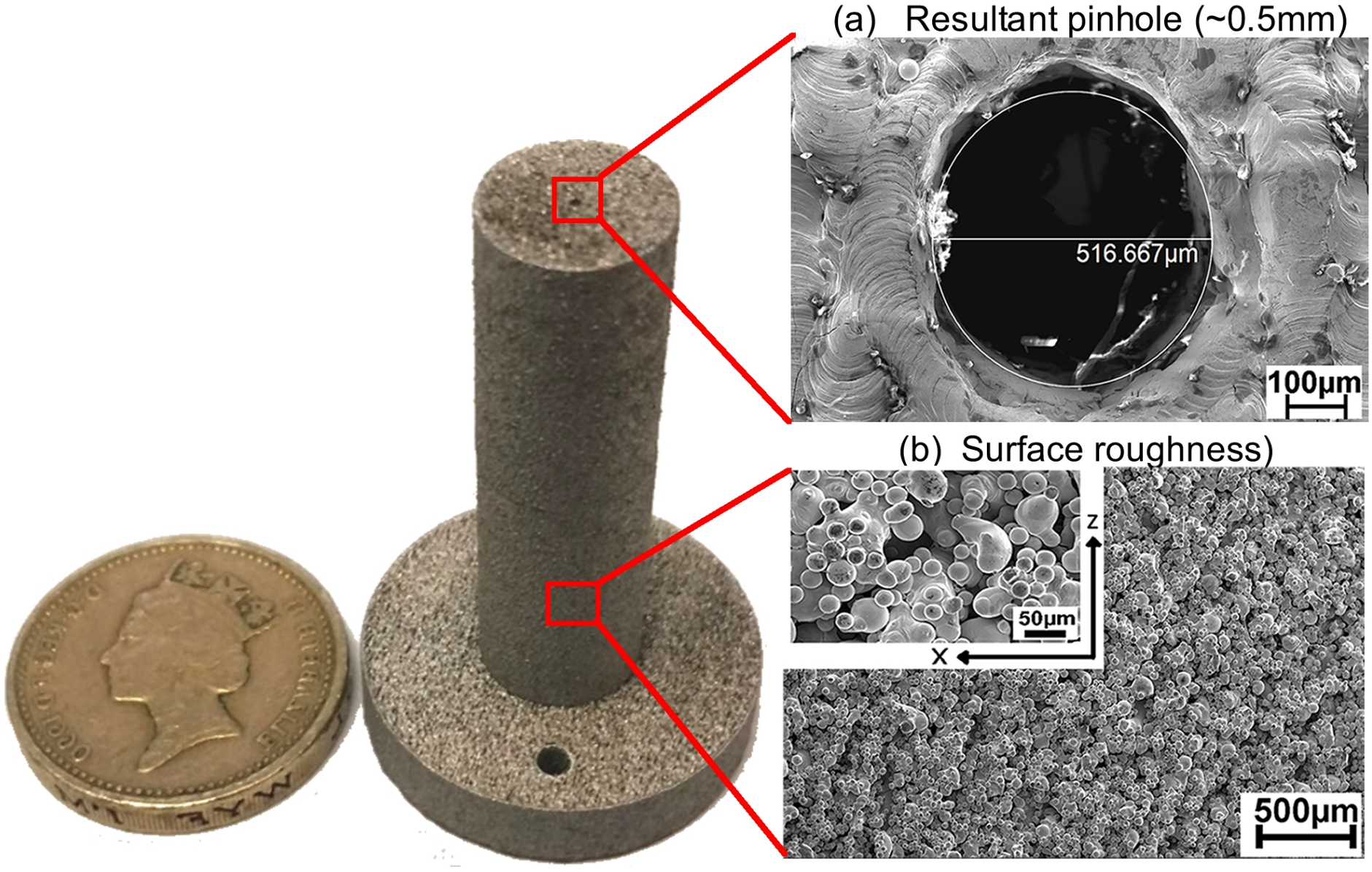
(a) Resultant pinhole (~0.5mm)
516.667μm
100μm
(b) Surface roughness)
Z
X
50μm
500μm

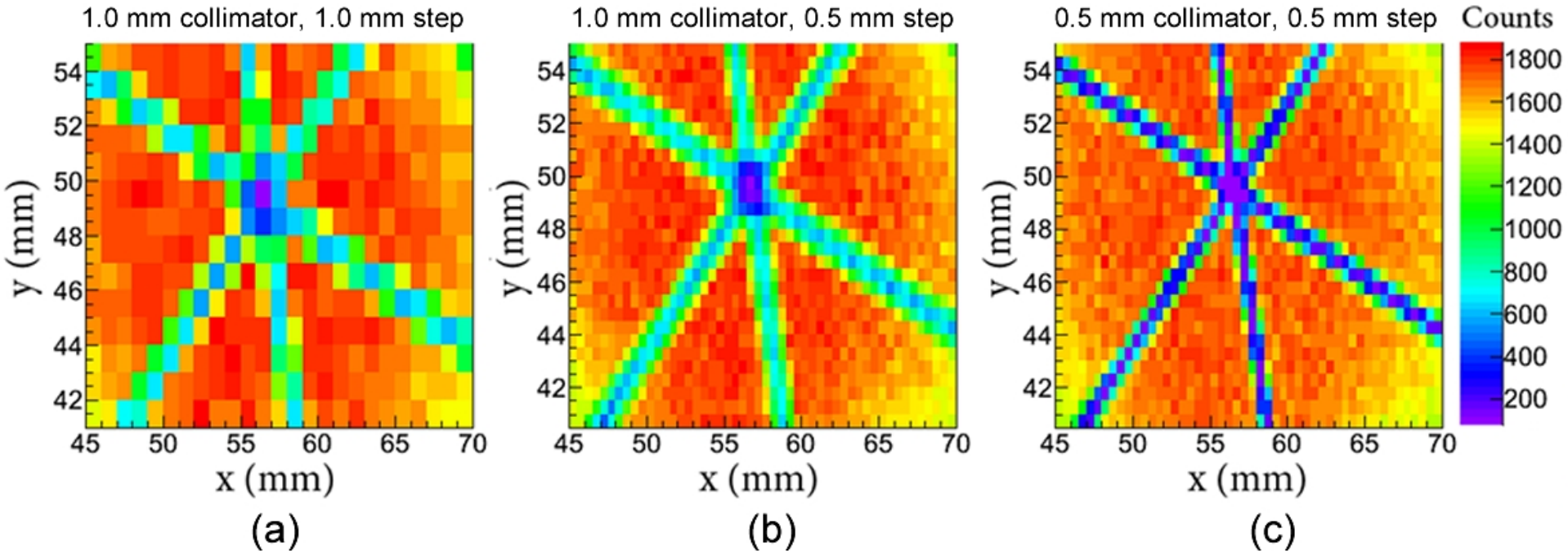
1.0 mm collimator, 1.0 mm step
1.0 mm collimator, 0.5 mm step
0.5 mm collimator, 0.5 mm step
Counts
1800
1600
1400
1200
1000
800
600
400
200
y (mm)
x (mm)
54
52
50
48
46
44
42
45
50
55
60
65
70
(a)
(b)
(c)

Physical properties	Tungsten
Density at 25 °C (g/cm^3)	19.2
Liquid Density (g/cm^3)	17.6
Melting Point (°C)	3422
Thermal Conductivity ($W.m^{-1}.K^{-1}$)	174
Melt Viscosity (mPa.s)	8
Ductile-to-brittle transition temperature – DBTT (°C)	250 to 400
Surface tension Force (N/m)	2.361

Table 1: Physical properties of tungsten Erik and Wolf-Dieter (1999; Paradis et al. (2005; Sidambe and Fox (2017; Sidambe et al. (2018; Zhou et al. (2015).

Hall Flow Test (sec/50g)	Tap Density (g/cm^3)	Apparent Density (g/cm^3)	Particle size distribution (μm)
5	12.1	10.9	D10=25.2 D50=33.7 D90=48.4

Table 2: The table shows the physical properties of the tungsten powder.

Elements	W	Al	Ta	Ti	O	Mo	Others, each
(wt%)	>99.9	0.001	0.003	0.001	0.009	0.003	<0.001

Table 3 - The table shows the chemical properties of the tungsten powder